3D bioprinting of a trachea-mimetic cellular construct of a clinically relevant size

Jeong Hun Park[a,1], Minjun Ahn[b,1], Sun Hwa Park[c,1], Hyeonji Kim[b], Mihyeon Bae[b], Wonbin Park[b], Scott J. Hollister[a,*], Sung Won Kim[c,*], Dong-Woo Cho[b,*]

[a]Wallace H. Coulter Department of Biomedical Engineering and Center for 3D Medical Fabrication, Georgia Institute of Technology and Emory University, 313 Ferst Drive, Atlanta, GA, 30332, USA

[b]Department of Mechanical Engineering, Pohang University of Science and Technology (POSTECH), 77 Cheongam-ro, Nam-gu, Pohang, Kyungbuk, 37673, Republic of Korea

[c]Department of Otolaryngology-Head and Neck Surgery, College of Medicine, The Catholic University of Korea, 222 Banpo-daero, Seocho-gu, 137-710, Republic of Korea

Abstract

Despite notable advances in extrusion-based 3D bioprinting, it remains a challenge to create a clinically-sized cellular construct using extrusion-based 3D printing due to long printing times adversely affecting cell viability and functionality. Here, we present an advanced extrusion-based 3D bioprinting strategy composed of a two-step printing process to facilitate creation of a trachea-mimetic cellular construct of clinically relevant size. A porous bellows framework is first printed using typical extrusion-based 3D printing. Selective printing of cellular components, such as cartilage rings and epithelium lining, is then performed on the outer grooves and

*Corresponding authors: Prof. Dong-Woo Cho, Ph.D. (dwcho@postech.ac.kr), Prof. Sung Won Kim, Ph.D. (kswent@catholic.ac.kr), Prof. Scott J. Hollister, Ph.D. (scott.hollister@bme.gatech.edu).
[1]These authors contributed equally to this work.

Author contributions

J.H.P. and M.A. designed research; J.H.P., M.A. S.H.P., H.K., J.-S.L., M.B., and W.P. performed research; S.J.H., S.W.K., and D.-W.C. supervised the research; J.H.P., M.A., and S.-H.P. analyzed the data and wrote the manuscript, and all authors discussed and reviewed the manuscript.

Credit author statement

Jeong Hun Park: Conceptualization, Data curation, Formal analysis, Investigation, Writing – original draft. **Minjun Ahn**: Conceptualization, Methodology, Data curation, Visualization, Writing – original draft. **Sun Hwa Park**: Methodology, Investigation, Visualization, Writing - original draft. **Hyeonji Kim**: Methodology, Visualization. **Mihyeon Bae**: Methodology, Data curation. **Wonbin Park**: Methodology, Investigation. **Scott J. Hollister**: Conceptualization, Supervision, Funding acquisition, Writing-Reviewing. **Sung Won Kim**: Conceptualization, Resources, Supervision, Funding acquisition, Writing- Reviewing. **Dong-Woo Cho**: Conceptualization, Supervision, Funding acquisition, Writing- Reviewing.

Declaration of competing interests

J.H.P., M.A., S.-H.P., J.-S.L., S.W.K., and D.-W.C. are inventors on a patent related to this work. The authors declare that they have no competing interests.

Declaration of interests

The authors declare that they have no known competing financial interests or personal relationships that could have appeared to influence the work reported in this paper.

inner surface of the bellows framework by a rotational printing process. With this strategy, 3D bioprinting of a trachea-mimetic cellular construct of clinically relevant size is achieved in significantly less total printing time compared to a typical extrusion-based 3D bioprinting strategy which requires printing of an additional sacrificial material. Tracheal cartilage formation was successfully demonstrated in a nude mouse model through a subcutaneous implantation study of trachea-mimetic cellular constructs wrapped with a sinusoidal-patterned tubular mesh preventing rapid resorption of cartilage rings *in vivo*. This two-step 3D bioprinting for a trachea-mimetic cellular construct of clinically relevant size can provide a fundamental step towards clinical translation of 3D bioprinting based tracheal reconstruction.

Keywords

3D bioprinting; trachea-mimetic cellular construct; clinically relevant size; tracheal cartilage regeneration

1. Introduction

Tissue engineered tracheal constructs are a potential solution for the reconstruction of long segment tracheal defects in which end-to-end anastomosis is not feasible [1, 2]. Various fabrication approaches, including extrusion-based 3D bioprinting, have been used to develop tracheal constructs with from different types of material and designs. In particular, printing of heterogenous constructs using multiple cell types and biocompatible polymers on extrusion-based 3D bioprinting has shown great potential in creating to create cellular tracheal constructs that recapitulate the biological and physiologic function of the native trachea [3–6].

On a typical extrusion-based 3D bioprinting system with the usual setup of the printing heads perpendicular to the build platform, a single heterogeneous construct containing multiple components is created through a layer-by-layer process using multiple printing heads that are independently controlled for printing each material [7, 8]. An additional printing head for sacrificial material must also be employed to support overhangs in the constructs being created. However, printing multiple components including support material on each layer is only feasible by sequential switching between printing heads, as only a single printing head can print a single component while the other printing heads are on standby. This very time-consuming switching between printing heads significantly increases the total printing time of a single construct composed of multiple components. Prolonged printing time causes significant problems in bioprinting results including low cell viability, loss of material integrity, and ultimately poor functionality of printed constructs [9–11]. It is imperative to shorten the total printing time of cell-containing components to ensure the cell viability and functionality for the creation of cellular constructs of clinically meaningful size.

Annular tracheal cartilage rings in the outer wall and tracheal mucosal epithelium on the luminal surface are the main tissue components critical to maintaining tracheal patency and normal function [12, 13]. Therefore, simultaneous regeneration of tracheal cartilage and epithelium should be achieved for ideal tracheal reconstruction that restores

tracheal structure and function using a cellular tracheal construct. Here, we present a clinically relevant sized trachea-mimetic cellular construct, composed of a porous bellows framework, separate cartilage rings on the outer grooves, and epithelium lining on the luminal surface of the bellows framework. The bellows framework was designed based on a canine tracheal anatomy to mimic the structural features and mechanical behavior of native trachea [14]. Finite element analysis (FEA) was then performed to determine the appropriate pore distribution to allow tissue ingrowth without compromising the mechanical integrity of the bellows framework. We also developed an advanced two-step extrusion-based 3D bioprinting strategy that significantly shortens the total printing time of a trachea-mimetic cellular construct of clinically relevant size. This approach first implemented direct extrusion-based 3D printing of a porous bellows framework from Poly-ε-caprolactone (PCL). Rotational printing of 3 % atelocollagen bioinks containing human nasal chondrocytes (hNCs) and human nasal turbinate stem cells (hNTSCs) was then implemented to selectively print separate cartilage rings on the outer grooves and epithelial lining on the luminal surface of the bellows framework without additional sacrificial materials. A schematic describing the two-step bioprinting process for the creation of a trachea-mimetic cellular construct of a clinically relevant size for tracheal reconstruction is presented in Fig. 1.

Furthermore, one of the important considerations in successful circumferential tracheal reconstruction is the *in vivo* environment to which the trachea-mimetic cellular construct will be exposed after end-to-end anastomosis implantation. The epithelial lining of the trachea-mimetic construct will be connected to the luminal epithelial tissue of the trachea at the anastomosis site while the cartilage rings will be directly exposed to surrounding muscle tissues, resulting in a potential rapid absorption of cartilage rings. Given that hydrogel retention has a close correlation with survival, expansion, and further tissue formation of encapsulated cells, a protective barrier between cartilage rings and surrounding muscle tissues should be implemented to prevent rapid resorption of cartilage rings after implantation [15, 16]. For this reason, we additionally devised a PCL sinusoidal-patterned tubular mesh (SPTM) to wrap the trachea-mimetic cellular construct before implantation. We then validated cartilage tissue formation capacity of a bioprinted trachea-mimetic cellular construct wrapped with a SPTM in the subcutaneous model in nude mice.

2. Methods

2.1. Materials

A thermoplastic polymer, poly-ε-caprolactone (PCL, Mw: 43,000 ~ 50,000, Polyscience Inc., USA), was used to print the porous bellows framework and STP mesh. Thermo-sensitive 3 % (w/v) atelocollagen based hydrogel (COLTRIX®, Ubiosis Inc., Korea) was used to prepare bioinks by encapsulating hNCs and hNTSCs for rotational printing of cartilage rings and epithelium lining, respectively.

2.2. Trachea-mimetic cellular construct design and FEA of bellows framework

A trachea-mimetic cellular construct composed of porous bellows framework, tracheal cartilage rings and epithelial lining was designed. The dimensions of bellows framework,

such as inner diameter, outer diameter, and longitudinal pitch between convolutions, were determined according to canine tracheal anatomy and dimensions [17]. Tracheal cartilage rings and epithelial lining were then added to the outer grooves between convolutions and the luminal surface of bellows framework, respectively.

The bellows framework should be porous for effective tracheal tissue infiltration. FEA was performed using FEBio version 2.9.1 (Febio.org) to determine appropriate pore distribution [18, 19]. The effect of pore distributions on the mechanical properties of bellows framework was analyzed under radical compression and three-point bending. The PCL bellows framework was modelled as a linear isotropic elastic material with a Young's modulus of 0.498 GPa and Poisson's ratio of 0.39. The properties of PCL used for FEA were obtained from tensile tests using PCL ASTM D638 Dumbbell shape specimens on a test machine (E42, MTS Systems Corporation, USA).

2.3. Extrusion-based 3D bioprinting of porous bellows framework

The porous bellows framework was created from PCL using the typical extrusion-based 3D bioprinting with a layer thickness of 100 μm. PCL grains were loaded into a 10 mL stainless steel syringe (SSY-10E, Musashi Engineering Inc., Japan) and melted at 80 °C. A molten PCL solution was extruded through a nozzle of 250 μm inner diameter by applying a pneumatic pressure of 500 kPa. The molten PCL was intermittently extruded under different printing head velocities (80 mm/min with extrusion and 305 mm/min without extrusion) in a pre-defined circular pathway to create approximately 300 μm pores in the wall.

2.4. Thermal incubation and oxygen plasma treatment

The printed porous bellows framework was thermally incubated for 30 min at 60 °C to increase structural integrity. Oxygen plasma treatment was also performed on the bellows frameworks at radio frequency of 50 kHz and power of 100 W for 120 min using a plasma reactor (CUTE, Femto Science Inc., Korea) to increase the hydrophilicity of the bellows framework surface.

2.5. Scanning electron microscopy

The PCL bellows frameworks, before and after thermal incubation, were coated with gold so as to observe the pore architecture on their surface using a scanning electron microscope (JSM-5300, JEOL, Japan) at an accelerating voltage of 15.0 kV.

2.6. Mechanical test

Radial compression and three-point bending tests were performed on the bellows frameworks as well as trachea-mimetic cellular constructs with and without SPTM wrapping using a universal mechanical testing machine (3340 Series Single Column Systems, Instron Corporation, USA) with a 2kN load cell. For three-point bending, two lower points were placed on the grooves at both ends of the bellows framework and the load was applied to the central convolution with a constant velocity of 0.2 mm/min. The load and displacement measured during the testing process were recorded.

2.7. Contact angle measurement

Contact angle on the surface of the PCL bellows framework before and after oxygen plasma treatment was measured using the sessile drop technique. 5 μL of distilled water was deposited on the inner and outer surface of the bellows framework in a controlled temperature and humidity (20 °C and 50 %). The angle of the drop against the plate was then evaluated using the measuring device (SmartDrop, FemtoBioMed co., Korea).

2.8. Cell isolation and culture

The hNCs and hNTSCs were isolated from the septum and inferior turbinate tissue following the procedures previously described [20, 21], which were approved by the Institutional Review Board of the ST. Mary's Hospital, Catholic University of Korea (KC08TISS0341). The isolated cells were seeded in a 75 mm2 cell culture flask (Gibco, USA). The hNCs and hNTSCs were then cultured in low-glucose Dulbecco's modified Eagle's medium (DMEM, Gibco, USA) with 10 % (v/v) fetal bovine serum (FBS, Gibco, USA) and 1% penicillin-streptomycin (Gibco, USA) at 37 °C in 5 % CO_2 incubator with a humidified atmosphere. The hNCs and hNTSCs were subcultured with a 1:3 ratio using 0.05 % (v/v) trypsin/EDTA solution (Gibco, USA) by six passages.

2.9. Bioink preparation

Cultured hNCs and hNTSCs were harvested, centrifuged at 1500 rev/min (rpm), and counted using a hemocytometer. The cell suspension with the determined number of cells was transferred to a conical tube and centrifuged again. The supernatant medium was aspirated and phosphate buffered saline (PBS) was added in 1/10 volume of 3 % (w/v) atelocollagen based hydrogel. Atelocollagen based hydrogel was then injected and gently mixed with the PBS cell suspension using positive displacement pipettes to ensure that cells were evenly distributed. All procedures working with atelocollagen based hydrogel were conducted under low temperature to avoid thermal gelation.

2.10. Rotational bioprinting of cartilage rings and epithelium lining

The porous bellows framework after thermal and oxygen plasma treatments was placed on the center of a motorized rotation stage (RMTS60-N, MiSuMi co., Japan) and revolved at a constant angular speed of 4 rpm. 3 % atelocollagen bioink containing hNCs was extruded through a 45 ° curved needle of 18 gauge (Musashi Engineering inc., Japan) and printed onto an outer groove during 1 revolution of the bellows framework to create a cartilage ring. This rotational printing process was repeated until cartilage rings were added onto all outer grooves.

For the rotational printing of the epithelial lining onto the luminal surface of the bellows framework, 3 % atelocollagen bioink containing hNTSCs was first printed onto the inner grooves and then the remaining inner surface of the bellows framework using a curved nozzle while the bellows framework was rotating.

2.11. Cell viability test

A live and dead cell viability kit (Invitrogen, USA) was used to analyze the effect of printing strategy on the cell viability. The trachea-mimetic cellular constructs created using typical extrusion-based printing and rotational printing were stained with calcein AM and ethidium homodimer solution, followed by incubation at 37 °C for 30 min. The stained cells were observed by a fluorescence microscope (Axiovert 200, Zeiss, Germany), and the proportion of live cells to total cells was calculated.

2.12. Contraction test

The trachea-mimetic cellular constructs printed with four different cell densities of hNCs and hNTSCs were cultured for 3 days *in vitro* and fixed with 4 % paraformaldehyde solution. After washing with PBS, each construct was cut into half, and the cross-sectional area of cartilage rings and epithelial lining was calculated using ImageJ software for quantitative analysis.

2.13. Gene expression analysis through Real-Time PCR

TRIzol reagent (Invitrogen, USA) was used to isolate total RNA from the trachea-mimetic cellular constructs according to the manufacturer's protocol. RNA concentration was then measured using Nanodrop (ND-2000, ThermoFisher Scientific co., USA). Reverse transcription was conducted by a cDNA synthesis kit (ThermoFisher Scientific co., USA) following the manufacturer's instructions. Gene expression was analyzed with SYBR-green (ThermoFisher Scientific co., USA) using 7500 Real-Time PCR device (Applied Biosystems, USA). The primers and probes for SOX9, ACAN, COL2, Mucin, Keratin-14, β-tubulin, and glyceraldehyde 3-phosphate dehydrogenase (GAPDH) were designed based on the published gene sequences (National Center for Biotechnology Information, USA). The analyses were conducted in triplicates and the fold changes of each gene expression level were calculated according to the 2- Ct method by normalizing to GAPDH. Sequences of the primers used in this study are represented in Table S1 of Supplementary Information.

2.14. Rotating rod combined 3D bioprinting of SPTM

A rotational rod combined 3D printing system (2RPS) was used to print the SPTM [22]. The rotating rod with a 0.5 mm diameter larger than the outer diameter of bellows framework was installed in the planar rotating system. The molten PCL solution was extruded under the same printing parameters as that of porous bellows framework and the tubular mesh with sinusoidal-pattern was created according to a pre-defined pathway of the printing head and rotation of the rotating rod.

2.15. Subcutaneous implantation

All procedures of the animal study were performed under the approval of Institutional Animal Care and Use Committee (IACUC), Pohang University of Science and Technology (POSTECH-2017–0099). BALB/c nude mice (6 weeks old, 26.5 ± 2.1 g, male) were randomly assigned into 2 experimental groups after an acclimation period of 2 weeks. A combination of 50 mg/kg ketamine hydrochloride (Yuhan co., Korea) and 3 mg/kg xylazine (Bayer Korea Ltd., Korea) were used to anesthetize the mice. Chlorohexidine was treated on

the dorsal skin and 70% ethanol was used for the aseptic preparation. A small skin incision (~ 15 mm) was made on the dorsal subcutaneous skin by blunt dissection. Scale-downed trachea-mimetic cellular constructs (5 mm inner diameter) with only cartilage rings were inserted into the incised space and placed above the muscle under the skin. The skin was then sutured with 4–0 silk for wound closure. The mouse was rehabilitated on a warm surgical bed until they awoke. At 8 weeks after implantation, the mice were sacrificed using CO_2 euthanasia and the implants were retrieved.

2.16. Histological and immunohistological analysis

The retrieved implants were cut in half longitudinally and fixed with 4 % paraformaldehyde solution. The fixed samples were then embedded in paraffin wax and sectioned into 25 μm thickness slices with a microtome. After deparaffinization, the sliced samples were treated with 0.5 % Triton X-100 solution (Biosesang co. Korea) for permeabilization. 1 % (w/v) bovine serum albumin (Sigma Aldrich, USA) solution was used to reduce the non-specific background. Sections were immunostained with a primary antibody against anti-Collagen II (Abcam, UK), and anti-Aggrecan (Abcam, UK) to make the cartilaginous ECM formation visible, followed by incubation with Alexa Flour secondary antibody (Invitrogen, USA) following the manufacturer's instructions. All samples were counterstained with DAPI (Vector Laboratories, USA). Stained samples were examined using a confocal microscope (LSM 8800, Zeiss, Germany).

For histological experiments, dewaxed sections were stained with staining kits for H&E (Abcam, UK), Alcian Blue (Abcam, UK), Safranin-O (ScienCell Research Laboratories co., USA), and Masson's Trichrome (Abcam, UK) following the manufacturer's instructions. Slides covered with cover-slips were scanned using an automatic digital slide scanner (Panoramic MIDI, 3DHISTECH, Hungary).

2.17. Statistical analysis

Quantitative data were represented as the mean ± SD. Statistical analysis was performed using two-tailed Student's t test to determine significant difference between two experimental groups. A one-way analysis of variance with Tukey's post hoc test was performed for multiple experimental groups. Differences were considered to be statistically significant when the p-value was less than 0.01. All experiments were performed five times (n=5).

3. Results

3.1. Mechanical behavior analysis of bellows framework

A bellows framework, the main body of the trachea-mimetic cellular construct that provides mechanical support with good patency, was designed based on canine tracheal anatomy [23, 24]. Since a bellows framework should have approximately 300 μm pores in the wall to allow ingrowth of epithelial tissue, FEA of the bellows framework was also performed to determine an appropriate pore distribution that maintains mechanical integrity of the bellows framework [25, 26]. FEA results showed that increasing pore density reduced radial stiffness and increased bending flexibility, but did not compromise the load-bearing capability

(Fig. 2A, B). The porous bellows framework was accordingly printed with 48 pores per circumference for better tissue ingrowth, which is the most compact pore distribution that can be feasibly printed using the extrusion-based 3D printing system in this study.

3.2. 3D printing of porous bellows framework

On a typical extrusion-based 3D printing system with the usual setup of printing heads perpendicular to the building platform, the bellows framework was printed by intermittent extrusion of molten PCL using different printing head velocities in a circular pathway, creating a wall thickness of 250 μm with distributed 300 μm pores (Fig. 2C, D). The porous bellows framework directly printed through a layer-by-layer process in a perpendicular direction showed significant variation in three-point bending response (Fig. 2E). Therefore, thermal incubation was performed to enhance the structural integrity of the porous bellows framework, producing a more consistent mechanical behavior without fracture under three-point bending while maintaining pore architecture (Fig. 2F–J). In addition, oxygen plasma treatment of the bellows framework was performed to improve hydrophilicity of the hydrophobic native PCL, allowing an increase in stability of the hydrogels printed on the outer grooves and luminal surface of the bellows framework. The contact angle of a water droplet on the framework surface decreased significantly from $82.4 \pm 4.5\,°$ to $48.6 \pm 3.2\,°$ (Fig. 2K, L).

3.3. Rotational printing of cartilage rings and epithelial lining

After printing of the porous bellows framework, rotational printing using 3 % atelocollagen bioinks containing hNCs and hNTSCs was performed to add separate cartilage rings onto the outer grooves and epithelial lining on the luminal surface of a bellows framework (Fig. 3A–C). Employing a curved nozzle enabled the extrusion of bioinks in a radial direction other than the perpendicular direction to the bellows framework revolving on the rotational stage, thereby eliminating the need for an additional printing head containing sacrificial material. Rotational printing was completed in 15 min while an estimated time for a typical printing strategy using 4 printing heads was more than 22 hours to create a trachea-mimetic cellular construct of clinically relevant size. A significantly higher cell viability was consequently confirmed with rotational printing in comparison with a typical extrusion-based printing strategy (Fig. 3D–F).

3.4. Appropriate cell density for cartilage rings and epithelial lining

We analyzed cell density effects on volume contraction, cell proliferation, and tissue formation after printing to determine an appropriate cell density for the cartilage rings and epithelial lining. Cartilage rings and epithelial lining printed with different cell densities of 1×10^6 cells/mL, 2×10^6 cells/mL, and 5×10^6 cells/mL maintained their initial volume, while cell density of 1×10^7 cells/mL showed a significant volume contraction in both after gelation (Fig. 4A, B). Further contraction was not observed at day 3 in any experimental groups (Fig. 4C, D). In cell proliferation analysis, both hNCs in the cartilage rings and hNTSCs in epithelial lining printed with cell density of 1×10^6 cells/mL, 2×10^6 cells/mL, and 5×10^6 cells/mL showed continuous proliferation through 7 days after printing while the cell density of 1×10^7 cells/mL showed reduced proliferation during the culture for 7 days (Fig. 4E, F). In addition, gene expression of cartilaginous markers including SOX9,

ACAN, and COL2 and epithelial differentiation markers including Musin, Keratin-14, and β-tubulin measured after 14 and 28 days of culturing were significantly higher in the cell density of 5×10^6 cells/mL compared to other cell densities (Fig. 4G–L). Taken together, these results suggested that a cell density of 5×10^6 cells/mL was the most appropriate for the printing of cartilage rings and epithelial lining of tracheal construct.

3.5. Resorption prevention of cartilage rings of tracheal construct in vivo

We applied the SPTM to wrap a trachea-mimetic cellular construct and prevent rapid resorption of cartilage rings *in vivo* without adversely affecting mechanical properties of the tracheal construct (Fig. 5A, B). An SPTM with 400 μm of gap between lines and 250 μm of wall thickness was printed from PCL using a rotating rod printing system [22]. We then analyzed the effect of the SPTM on the mechanical properties of trachea-mimetic cellular construct through mechanical testing using trachea-mimetic cellular constructs with or without SPTM. The load of the trachea-mimetic cellular construct with the SPTM was higher than that of the trachea-mimetic cellular construct without SPTM in both three-point bending and radial compression. The difference between two loads increased gradually as displacement increased; however, the difference was not significant over the whole range of displacement (Fig. 5C, D). A subcutaneous implantation study using nude mice was also performed to validate the effect of SPTM on the resorption of cartilage rings *in vivo* (Fig. 5E). At 8 weeks after implantation, cartilage rings of the trachea-mimetic construct without the SPTM were almost completely resorbed while those of trachea-mimetic construct with SPTM successfully retained their initial volume without severe resorption (Fig. 5F–I). The cross-sectional area of cartilage rings from the trachea-mimetic constructs without an SPTM was $52.05 \pm 2.59\%$ of the initial area as compared to $94.05 \pm 2.59\%$ with an SPTM (Fig. 5J).

3.6. Tracheal cartilage formation of tracheal construct in vivo

The longitudinal cross-sectional area of cartilage rings was stained with H&E, Alcian Blue (AB), Safranin-O, and Masson's Trichrome (MT). H&E staining results indicated that mature round-shaped chondrocytes were embedded in lacunae-like spaces inside abundant extracellular matrix (ECM) in the trachea-mimetic constructs with SPTM whereas less ECM was presented with chondrocytes of fibroblast-like morphology in the trachea-mimetic constructs without SPTM (Fig. 6A, B). Intense staining of AB and Safranin-O confirmed the abundant sulfated glycosaminoglycan (sGAG) in the newly generated cartilage tissue in the group of trachea-mimetic constructs with SPTM (Fig. 6C–F). The presence of abundant total collagen was also confirmed by intense staining of MT in trachea-mimetic construct with the SPTM group (Fig. 6G, H). Cartilaginous ECM including collagen type II (COL2) and aggrecan (ACAN) were observed only in the trachea-mimetic construct with SPTM, which indicates that implementation of SPTM allowed higher cell viability and further tissue formation by preventing rapid resorption of the cartilage rings of the trachea-mimetic constructs *in vivo* (Fig. 6I, J).

4. Discussion

Extrusion-based 3D bioprinting with multiple printing heads is a powerful tool for creating heterogenous cellular constructs that recapitulate biological and physiological

features of native tissues using various cell types and biocompatible polymers [27–29]. However, typical extrusion-based 3D bioprinting, with the usual setup of the printing heads perpendicular to the build platform, still has limited printing speed [30], which adversely affects cell viability and cell functionality, including differentiation and ECM formation. This limitation can be improved by increasing printing head velocity with larger sized nozzles or minimizing the printing path of each printing head; however, these modifications may have an adverse effect on printing quality and cannot fundamentally overcome the printing speed limitation. Extrusion-based 3D bioprinting should continue to evolve to shorten printing time given that large size cellular constructs are required to address realistic clinical reconstruction needs.

In order to create the trachea-mimetic cellular construct using the typical extrusion-based 3D bioprinting system setup, three printing components for bellows framework, cartilage rings and epithelial lining are required. Aside from these, an additional sacrificial material printing must be employed to avoid of the printed bioinks for cartilage rings and epithelial lining flowing into other areas during the printing process before gelation. Each printing component should be alternatively printed by a time-consuming switching between four printing heads and the final construct is achieved by selectively dissolving the sacrificial material after printing (Fig. S1A–N, Supplementary Information). Additional sacrificial material printing and time-consuming switching between printing heads leads to a significant increase in printing time. Approximately 22 hours of printing time was estimated by the printing system software. Given that nutrition cannot be supplied to the cells through the medium during the printing process, an adverse effect from this prolonged printing time on the cell viability is inevitable.

We developed an advanced extrusion-based 3D bioprinting strategy consisting of a two-step process to enable rapid creation of the trachea-mimetic cellular construct of a clinically relevant size. First, a porous bellows framework for the trachea-mimetic cellular construct was created through a typical layer-by-layer process. This process takes fundamental advantage of 3D bioprinting in that it allows high flexibility in the dimensions of the bellows framework, which is essential for customized design according to the patient's anatomy. Cellular components such as cartilage rings and epithelial lining were then selectively added through a rotational printing process using a rotational stage and a curved nozzle. Employing a curved nozzle enabled the extrusion of bioinks in a radial direction other than the perpendicular direction toward the bellows framework revolving on the rotational stage. Rotational printing successfully enabled rapid, independent, and sequential printing of separate cartilage rings and epithelium lining on the bellows framework without additional printing of sacrificial material. Total rotational printing time of cartilage rings and epithelium lining was 15 min while approximately 22 hours was estimated to create a trachea-mimetic cellular construct through a layer-by-layer process using typical extrusion-based 3D printing with four separate printing heads for PCL, cartilage component, epithelium component, and sacrificial material. We confirmed that a significant decrease in printing time leads to significantly enhanced cell viability and functionality of the trachea-mimetic cellular construct, including differentiation capacity into tracheal cartilage and epithelial tissues.

We selected PCL to print a porous bellows framework and SPTM since PCL is one of the most widely used biomaterials in medical implant development with good printability [31, 32]. Even though the PCL bellows framework has higher stiffness than native trachea due to the relatively stiff mechanical properties of PCL (Fig. S2A–F, Supplementary Information), PCL is one of the reliable biocompatible polymers that have been approved by the US Food and Drug Administration (FDA) for clinical use. Its safety has been demonstrated clinically by a number of medical devices and tissue reconstruction implants [32–34]. However, extrusion-based 3D bioprinting of porous bellows framework from PCL has inherent limitations, such as poor hydrophilicity and variable mechanical properties with lower fracture strength, to be used as a framework for the cellular tracheal construct [35, 36]. Poor hydrophilicity of PCL led to the detachment of the cartilage rings from the bellows framework during *in vitro* culture (Fig. S3A, B, Supplementary Information). Furthermore, extrusion-based 3D bioprinting through a layer-by-layer process with intermittent extrusion of the PCL to create the porous bellows framework resulted in lower fracture strength as well as significant variation in mechanical behavior of the bellows framework. These limitations reduce quality and reproducibility of a cellular tracheal construct for clinical applications. In order to overcome those limitations, additional treatments, such as thermal incubation and oxygen plasma treatment, were applied to the PCL bellows framework prior to rotational printing of cellular components [37–39]. In particular, thermal incubation enhanced the structural integrity by allowing the PCL layers directly printed in a layer-by-layer fashion to bond more strongly while maintaining pore architecture, thereby leading to an increase in mechanical reliability among the final products. The implementation of additional treatments between two printing processes is also another advantage of an advanced extrusion-based 3D bioprinting strategy that is not feasible on typical extrusion-based 3D bioprinting with multiple printing heads. Moreover, printing of the bellows framework prior to rotational printing of cellular components has the significant potential to enable an off-the-shelf approach for cellular constructs. Bellows frameworks printed with different dimensions in advance can be stored in appropriate conditions and be ready-to-use for further printing of cellular component as needed. A trachea-mimetic cellular construct can be rapidly prepared from the designated bellows framework with appropriate dimensions according to the patient's anatomical information and it can be provided to the patient in a short time.

In this study, we used hNCs- and hNTSCs-laden collagen hydrogels as bioinks for the printing of cartilage rings and epithelial lining, respectively. Our ultimate goal is the clinical application of the trachea-mimetic cellular construct created using this advanced extrusion-based 3D bioprinting strategy, and we selected a commercialized collagen hydrogel that has been used in clinical applications [40–42]. Cell density, along with hydrogel concentration, is one of the most important factors in determining the biomechanical and biochemical properties of cell-laden hydrogels, including contraction, cell proliferation, ECM formation and reorganization [43, 44]. We also believe that cell density is an important factor for given collagen hydrogel concentrations in determining the appropriate preparation time and consequent performance of cellular tracheal constructs clinically. In this regard, we analyzed the effect of cell density on contraction as well as further cell viability and functionality, such as differentiation potential of cellular components of the tracheal construct into tracheal

cartilage and epithelial tissue. It has been well known that rheological properties and printability of cell-laden hydrogel vary according to the cell density within the hydrogel [45, 46]. However, we assumed that the amount of bioink extruded through a curved nozzle would be primarily influenced by bioink concentration rather than cell density since the curved nozzle used for printing of bioinks with different cell densities is sufficiently large to allow bioink flow (0.838 mm of inner diameter) [47]. All bioinks for the cell density effect analysis were printed using the same printing parameters and a relative comparison study of contraction and further cellular activities was performed.

We confirmed that a cell density of 5×10^6 cells/ml was the most effective in volume retention, cell proliferation, and tissue formation *in vitro* for both the cartilage rings and epithelium lining of the tracheal construct. The highest cell density of 1×10^7 cells/ml exhibited severe contraction during the gelation, which was caused by the increased traction force of cells under excessive cell-cell and cell-fibrils interactions compared to other experimental groups with lower cell densities [48, 49]. This contraction at the highest cell density increased collagen density and inhibited cell proliferation over 7 days in culture. Furthermore, rapid contact-inhibition induced by disrupted intercellular communication at the highest cell density would have contributed to inhibition of cell proliferation as well as limited cell differentiation into cartilage and epithelial tissues [49–51]. Other cell densities lower than 5×10^6 cells/ml also exhibited a consistent increase in cell proliferation and differentiation. However, they are likely to need more time to reach similar cell proliferation and gene expression levels to those of cell density of 5×10^6 cells/ml. Given that the trachea-mimetic cellular construct should be prepared in time, we concluded that 5×10^6 cells/ml of cell density is optimal for creation of cellular tracheal constructs.

The subcutaneous model in nude mice was employed to mimic the *in vivo* environment to which cartilage rings of the trachea-mimetic cellular construct will be exposed. In circumferential tracheal reconstruction, no cell migration from surrounding cartilage tissue can be expected and the use of chondrocytes or other cell sources are fundamental to regenerate tracheal cartilage rings following end-to-end anastomosis implantation [52, 53]. In this study, cartilage rings of the cellular tracheal construct were composed of a collagen hydrogel in with hNCs at a cell density of 5×10^6 cells/mL. However, those cartilage rings, having large outer surface area, will be directly exposed to surrounding muscle tissue after implantation and a protective barrier between the surrounding muscle and printed cartilage is required to prevent rapid resorption of cartilage rings *in vivo* [54, 55]. In this study, a SPTM was applied to wrap the tracheal construct. The cartilage rings within the SPTM successfully maintained their initial volume for 2 months after implantation. Retention of collagen hydrogel with optimal hNCs density by the SPTM significantly facilitated cartilage formation *in vivo*. Numerous infiltrated microvessels were also found around the regenerated cartilage tissue, indicating successful integration with surrounding native tissue (Fig. S4, Supplementary Information). Furthermore, sinusoidal-pattern in the wall provided the SPTM bending flexibility without changes in patency, and it was demonstrated that the application of SPTM does not adversely affect mechanical properties and behavior of the tracheal construct. The application of a protective mesh therefore should be considered essential to protect the cartilage rings of the trachea-mimetic cellular construct. Meanwhile, the SPTM design parameters including line width, wall thickness and gap between the lines

will influence the mechanical properties of the SPTM as well as the trachea-mimetic cellular construct wrapped with SPTM. It can also be expected that the amount and rate of cartilage ring resorption will be affected by these design parameters of the SPTM. In this regard, optimizing the SPTM design parameters in regard to their effect on mechanical properties as well as the amount and rate of cartilage ring resorption also needs to be performed to further enhance SPTM performance.

In this study, we developed a two-step 3D bioprinting strategy to create a trachea-mimetic cellular construct with appropriate cell density and high viability. We also validated the cartilage regeneration capacity of the trachea-mimetic cellular construct using a nude mouse model since subcutaneous implantation provides no cell migration from surrounding cartilage tissue, similar to the *in vivo* environment after implantation into a circumferential tracheal defect. Although the epithelial regeneration capacity of the tracheal construct was not validated in this study, we believe that complete tracheal epithelium can be successfully achieved on the luminal surface of the tracheal construct based on our previous studies [56, 57]. Future work will include the *in vivo* validation of a cellular tracheal construct of clinically relevant size in large animal models in terms of simultaneous regeneration capacity of tracheal cartilage and epithelial tissue, as well as mechanical and structural stability.

Supplementary Material

Refer to Web version on PubMed Central for supplementary material.

Acknowledgements

References

[1]. Luo X, Liu Y, Zhang Z, Tao R, Liu Y, He A, Yin Z, Li D, Zhang W, Liu W, Long-term functional reconstruction of segmental tracheal defect by pedicled tissue-engineered trachea in rabbits, Biomaterials 34(13) (2013) 3336–3344. [PubMed: 23380355]

[2]. Dhasmana A, Singh A, Rawal S, Biomedical grafts for tracheal tissue repairing and regeneration "Tracheal tissue engineering: an overview", Journal of Tissue Engineering and Regenerative Medicine (2020).

[3]. Bae S-W, Lee K-W, Park J-H, Lee J, Jung C-R, Yu J, Kim H-Y, Kim D-H, 3D bioprinted artificial trachea with epithelial cells and chondrogenic-differentiated bone marrow-derived mesenchymal stem cells, International journal of molecular sciences 19(6) (2018) 1624.

[4]. Ke D, Yi H, Est-Witte S, George S, Kengla C, Lee SJ, Atala A, Murphy SV, Bioprinted trachea constructs with patient-matched design, mechanical and biological properties, Biofabrication 12(1) (2019) 015022. [PubMed: 31671417]

[5]. Kim SH, Yeon YK, Lee JM, Chao JR, Lee YJ, Seo YB, Sultan MT, Lee OJ, Lee JS, S.-i. Yoon, Precisely printable and biocompatible silk fibroin bioink for digital light processing 3D printing, Nature communications 9(1) (2018) 1–14.

[6]. Gao M, Zhang H, Dong W, Bai J, Gao B, Xia D, Feng B, Chen M, He X, Yin M, Tissue-engineered trachea from a 3D-printed scaffold enhances whole-segment tracheal repair, Scientific reports 7(1) (2017) 1–12. [PubMed: 28127051]

[7]. Jiang Z, Diggle B, Tan ML, Viktorova J, Bennett CW, Connal LA, Extrusion 3D Printing of Polymeric Materials with Advanced Properties, Advanced Science 7(17) (2020) 2001379. [PubMed: 32999820]

[8]. Kim BS, Ahn M, Cho W-W, Gao G, Jang J, Cho D-W, Engineering of diseased human skin equivalent using 3D cell printing for representing pathophysiological hallmarks of type 2 diabetes in vitro, Biomaterials 272 (2021) 120776. [PubMed: 33798956]

[9]. Placone JK, Engler AJ, Recent Advances in Extrusion- Based 3D Printing for Biomedical Applications, Advanced healthcare materials 7(8) (2018) 1701161.

[10]. Prendergast ME, Burdick JA, Recent advances in enabling technologies in 3D printing for precision medicine, Advanced Materials 32(13) (2020) 1902516.

[11]. Idaszek J, Costantini M, Karlsen TA, Jaroszewicz J, Colosi C, Testa S, Fornetti E, Bernardini S, Seta M, Kasarełło K, 3D bioprinting of hydrogel constructs with cell and material gradients for the regeneration of full-thickness chondral defect using a microfluidic printing head, Biofabrication 11(4) (2019) 044101. [PubMed: 31151123]

[12]. Crowley C, Birchall M, Seifalian AM, Trachea transplantation: from laboratory to patient, Journal of tissue engineering and regenerative medicine 9(4) (2015) 357–367. [PubMed: 26052583]

[13]. Li D, Yin Z, Liu Y, Feng S, Liu Y, Lu F, Xu Y, Min P, Hou M, Li K, Regeneration of trachea graft with cartilage support, vascularization, and epithelization, Acta Biomaterialia 89 (2019) 206–216. [PubMed: 30867137]

[14]. Park JH, Hong JM, Ju YM, Jung JW, Kang H-W, Lee SJ, Yoo JJ, Kim SW, Kim SH, Cho D-W, A novel tissue-engineered trachea with a mechanical behavior similar to native trachea, Biomaterials 62 (2015) 106–115. [PubMed: 26041482]

[15]. Martin JR, Patil P, Yu F, Gupta MK, Duvall CL, Enhanced stem cell retention and antioxidative protection with injectable, ROS-degradable PEG hydrogels, Biomaterials 263 (2020) 120377. [PubMed: 32947094]

[16]. Zhao N, Yue Z, Cui J, Yao Y, Song X, Cui B, Qi X, Han Z, Han Z-C, Guo Z, IGF-1C domain-modified hydrogel enhances therapeutic potential of mesenchymal stem cells for hindlimb ischemia, Stem cell research & therapy 10(1) (2019) 1–12. [PubMed: 30606242]

[17]. Kara ME, Turan E, Dabanoglu I, Ocal MK, Computed tomographic assessment of the trachea in the German shepherd dog, Annals of Anatomy-Anatomischer Anzeiger 186(4) (2004) 317–321.

[18]. Maas SA, Ateshian GA, Weiss JA, FEBio: history and advances, Annual review of biomedical engineering 19 (2017) 279–299.

[19]. Maas SA, Ellis BJ, Ateshian GA, Weiss JA, FEBio: finite elements for biomechanics, Journal of biomechanical engineering 134(1) (2012).

[20]. Kim DH, Lim JY, Kim SW, Lee W, Park SH, Kwon MY, Park SH, Lim MH, Back SA, Yun BG, Characteristics of Nasal Septal Cartilage–Derived Progenitor Cells during Prolonged Cultivation, Otolaryngology–Head and Neck Surgery 159(4) (2018) 774–782. [PubMed: 29787348]

[21]. Hwang SH, Kim SY, Park SH, Choi MY, Kang HW, Seol Y-J, Park JH, Cho D-W, Hong OK, Rha JG, Human inferior turbinate: an alternative tissue source of multipotent mesenchymal stromal cells, Otolaryngology--Head and Neck Surgery 147(3) (2012) 568–574. [PubMed: 22588732]

[22]. Ha D-H, Kim JY, Park TS, Park JH, Chae S, Kim BS, Lee HC, Cho D-W, Development of a radiopaque, long-term drug eluting bioresorbable stent for the femoral-iliac artery, RSC advances 9(59) (2019) 34636–34641.

[23]. Dabano lu I, Öcal M, Kara M, A quantitative study on the trachea of the dog, Anatomia, histologia, embryologia 30(1) (2001) 57–59.

[24]. Lee J.S.-j., Park J, Shin D-A, Ryu Y.-j., Kim HC, Lee JC, Kwon SK, Characterization of the biomechanical properties of canine trachea using a customized 3D-printed apparatus, Auris Nasus Larynx 46(3) (2019) 407–416. [PubMed: 30392980]

[25]. Sekine T, Nakamura T, Matsumoto K, Liu Y, Ueda H, Tamura N, Shimizu Y, Carinal reconstruction with a Y-shaped collagen-conjugated prosthesis, The Journal of Thoracic and Cardiovascular Surgery 119(6) (2000) 1162–1168. [PubMed: 10838533]

[26]. Omori K, Tada Y, Suzuki T, Nomoto Y, Matsuzuka T, Kobayashi K, Nakamura T, Kanemaru S, Yamashita M, Asato R, Clinical application of in situ tissue engineering using a scaffolding

technique for reconstruction of the larynx and trachea, Annals of Otology, Rhinology & Laryngology 117(9) (2008) 673–678.

[27]. Kang H-W, Lee SJ, Ko IK, Kengla C, Yoo JJ, Atala A, A 3D bioprinting system to produce human-scale tissue constructs with structural integrity, Nature biotechnology 34(3) (2016) 312–319.

[28]. Kim BS, Das S, Jang J, Cho D-W, Decellularized extracellular matrix-based bioinks for engineering tissue-and organ-specific microenvironments, Chemical Reviews 120(19) (2020) 10608–10661. [PubMed: 32786425]

[29]. Pati F, Jang J, Ha D-H, Kim SW, Rhie J-W, Shim J-H, Kim D-H, Cho D-W, Printing three-dimensional tissue analogues with decellularized extracellular matrix bioink, Nature communications 5(1) (2014) 1–11.

[30]. Tumbleston JR, Shirvanyants D, Ermoshkin N, Janusziewicz R, Johnson AR, Kelly D, Chen K, Pinschmidt R, Rolland JP, Ermoshkin A, Continuous liquid interface production of 3D objects, Science 347(6228) (2015) 1349–1352. [PubMed: 25780246]

[31]. Yun W-S, Shim J-H, Park K-H, Choi D, Park MI, Hwang SH, Kim SW, Clinical application of 3-dimensional printing technology for patients with nasal septal deformities: a multicenter study, JAMA Otolaryngology–Head & Neck Surgery 144(12) (2018) 1145–1152. [PubMed: 30326042]

[32]. Han HH, Shim J-H, Lee H, Kim BY, Lee J-S, Jung JW, Yun W-S, Baek CH, Rhie J-W, Cho D-W, Reconstruction of complex maxillary defects using patient-specific 3D-printed biodegradable scaffolds, Plastic and Reconstructive Surgery Global Open 6(11) (2018).

[33]. Pati F, Ha D-H, Jang J, Han HH, Rhie J-W, Cho D-W, Biomimetic 3D tissue printing for soft tissue regeneration, Biomaterials 62 (2015) 164–175. [PubMed: 26056727]

[34]. Morrison RJ, Hollister SJ, Niedner MF, Mahani MG, Park AH, Mehta DK, Ohye RG, Green GE, Mitigation of tracheobronchomalacia with 3D-printed personalized medical devices in pediatric patients, Science translational medicine 7(285) (2015) 285ra64–285ra64.

[35]. Zhu Y, Gao C, Shen J, Surface modification of polycaprolactone with poly (methacrylic acid) and gelatin covalent immobilization for promoting its cytocompatibility, Biomaterials 23(24) (2002) 4889–4895. [PubMed: 12361630]

[36]. Zhao L, Ma S, Pan Y, Zhang Q, Wang K, Song D, Wang X, Feng G, Liu R, Xu H, Functional modification of fibrous PCL scaffolds with fusion protein VEGF- HGFI enhanced cellularization and vascularization, Advanced healthcare materials 5(18) (2016) 2376–2385. [PubMed: 27391702]

[37]. Lee SJ, Oh SH, Liu J, Soker S, Atala A, Yoo JJ, The use of thermal treatments to enhance the mechanical properties of electrospun poly (ε-caprolactone) scaffolds, Biomaterials 29(10) (2008) 1422–1430. [PubMed: 18096219]

[38]. Yildirim ED, Besunder R, Guceri S, Allen F, Sun W, Fabrication and plasma treatment of 3D polycaprolactane tissue scaffolds for enhanced cellular function, Virtual and Physical Prototyping 3(4) (2008) 199–207.

[39]. Martins A, Pinho ED, Faria S, Pashkuleva I, Marques AP, Reis RL, Neves NM, Surface modification of electrospun polycaprolactone nanofiber meshes by plasma treatment to enhance biological performance, small 5(10) (2009) 1195–1206. [PubMed: 19242938]

[40]. Shetty A, Kim S, Alva K, Ahmed S, A single-stage arthroscopic treatment of articular cartilage defects: autologous collagen-induced chondrogenesis.(ACIC: shetty-Kim Technique) five-year results, Orthopaedic Proceedings, The British Editorial Society of Bone & Joint Surgery, 2017, pp. 9–9.

[41]. Shaikh N, Seah MK, Khan WS, Systematic review on the use of autologous matrix-induced chondrogenesis for the repair of articular cartilage defects in patients, World Journal of Orthopedics 8(7) (2017) 588. [PubMed: 28808630]

[42]. Seong H, Kim RK, Shin Y, Lee HW, Koh JC, Application of purified porcine collagen in patients with chronic refractory musculoskeletal pain, The Korean Journal of Pain 33(4) (2020) 395. [PubMed: 32989204]

[43]. Bitar M, Brown RA, Salih V, Kidane AG, Knowles JC, Nazhat SN, Effect of cell density on osteoblastic differentiation and matrix degradation of biomimetic dense collagen scaffolds, Biomacromolecules 9(1) (2008) 129–135. [PubMed: 18095652]

[44]. Puetzer JL, Bonassar LJ, High density type I collagen gels for tissue engineering of whole menisci, Acta biomaterialia 9(8) (2013) 7787–7795. [PubMed: 23669622]

[45]. Diamantides N, Dugopolski C, Blahut E, Kennedy S, Bonassar LJ, High density cell seeding affects the rheology and printability of collagen bioinks, Biofabrication 11(4) (2019) 045016.

[46]. Billiet T, Gevaert E, De Schryver T, Cornelissen M, Dubruel P, The 3D printing of gelatin methacrylamide cell-laden tissue-engineered constructs with high cell viability, Biomaterials 35(1) (2014) 49–62. [PubMed: 24112804]

[47]. Gillispie GJ, Han A, Uzun-Per M, Fisher J, Mikos AG, Niazi MKK, Yoo JJ, Lee SJ, Atala A, The Influence of Printing Parameters and Cell Density on Bioink Printing Outcomes, Tissue Engineering Part A 26(23–24) (2020) 1349–1358. [PubMed: 32928068]

[48]. Cross VL, Zheng Y, Choi NW, Verbridge SS, Sutermaster BA, Bonassar LJ, Fischbach C, Stroock AD, Dense type I collagen matrices that support cellular remodeling and microfabrication for studies of tumor angiogenesis and vasculogenesis in vitro, Biomaterials 31(33) (2010) 8596–8607. [PubMed: 20727585]

[49]. Zhou H, Weir MD, Xu HH, Effect of cell seeding density on proliferation and osteodifferentiation of umbilical cord stem cells on calcium phosphate cement-fiber scaffold, Tissue Engineering Part A 17(21–22) (2011) 2603–2613. [PubMed: 21745111]

[50]. Warne DJ, Baker RE, Simpson MJ, Optimal quantification of contact inhibition in cell populations, Biophysical journal 113(9) (2017) 1920–1924. [PubMed: 29032961]

[51]. Puliafito A, Hufnagel L, Neveu P, Streichan S, Sigal A, Fygenson DK, Shraiman BI, Collective and single cell behavior in epithelial contact inhibition, Proceedings of the National Academy of Sciences 109(3) (2012) 739–744.

[52]. Gao B, Jing H, Gao M, Wang S, Fu W, Zhang X, He X, Zheng J, Long-segmental tracheal reconstruction in rabbits with pedicled Tissue-engineered trachea based on a 3D-printed scaffold, Acta biomaterialia 97 (2019) 177–186. [PubMed: 31352107]

[53]. Xu Y, Li D, Yin Z, He A, Lin M, Jiang G, Song X, Hu X, Liu Y, Wang J, Tissue-engineered trachea regeneration using decellularized trachea matrix treated with laser micropore technique, Acta biomaterialia 58 (2017) 113–121. [PubMed: 28546133]

[54]. Malaise S, Rami L, Montembault A, Alcouffe P, Burdin B, Bordenave L, Delmond S, David L, Bioresorption mechanisms of chitosan physical hydrogels: a scanning electron microscopy study, Materials Science and Engineering: C 42 (2014) 374–384. [PubMed: 25063131]

[55]. Berdichevski A, Shachaf Y, Wechsler R, Seliktar D, Protein composition alters in vivo resorption of PEG-based hydrogels as monitored by contrast-enhanced MRI, Biomaterials 42 (2015) 1–10. [PubMed: 25542788]

[56]. Park JH, Park JY, Nam I-C, Ahn M, Lee JY, Choi SH, Kim SW, Cho D-W, A rational tissue engineering strategy based on three-dimensional (3D) printing for extensive circumferential tracheal reconstruction, Biomaterials 185 (2018) 276–283. [PubMed: 30261427]

[57]. Park JH, Park JY, Nam I-C, Hwang S-H, Kim C-S, Jung JW, Jang J, Lee H, Choi Y, Park SH, Human turbinate mesenchymal stromal cell sheets with bellows graft for rapid tracheal epithelial regeneration, Acta biomaterialia 25 (2015) 56–64. [PubMed: 26163763]
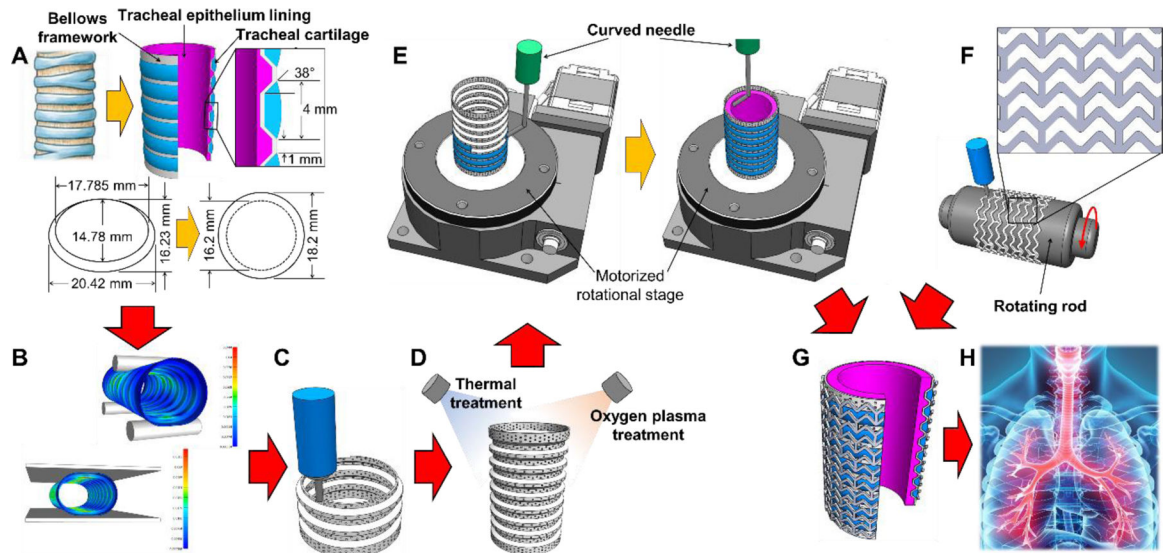
Fig. 1.
Schematics of the advanced two-step extrusion-based 3D bioprinting of the trachea-mimetic cellular construct of clinically relevant size. Step 1: (A) Design of the trachea-mimetic cellular construct based on canine tracheal anatomy. (B) FEA determining the effect of pore distribution on the mechanical behavior of the bellows framework. (C) Creation of porous bellows framework using a typical extrusion-based 3D printing. (D) Thermal/oxygen plasma treatments on the printed bellows framework. Step 2: (E) Rotational printing of separate cartilage rings and epithelial lining on the outer grooves and on the luminal surface of the bellows framework. (F) Creation of a SPTM for prevention of rapid resorption of cartilage rings *in vivo*. (G) Wrapping the trachea-mimetic cellular construct with a SPTM. (H) Implantation of the trachea-mimetic cellular construct wrapped with a SPTM into the circumferential tracheal defect for simultaneous regeneration of tracheal cartilage and epithelium.
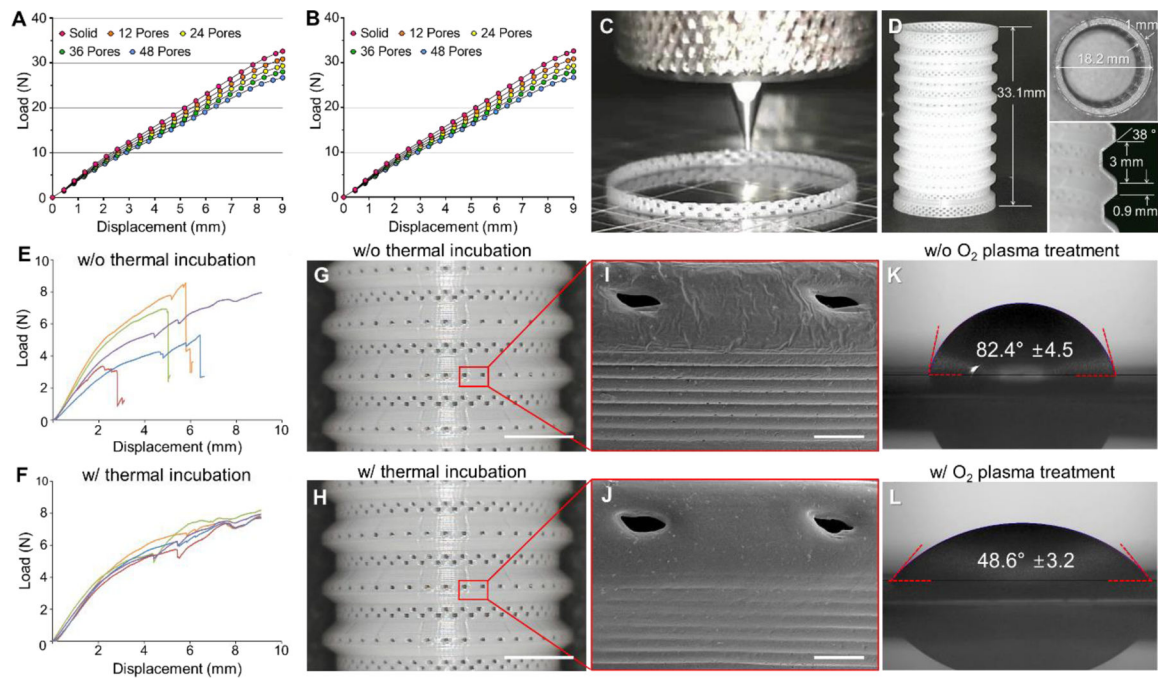
Fig. 2.
Mechanical behavior analysis and extrusion-based 3D bioprinting of bellows frameworks. FEA load-displacement curves of bellows framework having different pore distributions under (A) radial compression and (B) three-point bending. (C) Photograph of typical extrusion-based printing process of porous bellows framework. (D) Printing results of porous bellows framework of clinically relevant size. Load-displacement curves of porous bellows framework under three-point bending (E) before and (F) after thermal incubation. Photographs of the PCL bellows framework (G) before and (H) after thermal incubation. Scale bars, 5 mm. SEM images of the red box in each photograph of bellows framework (I) before and (J) after thermal incubation for pore architecture observation. Scale bars, 500 μm. Contact angle of water droplet on the outer surface of bellows framework (K) before oxygen plasma treatment and (L) after oxygen plasma treatment.
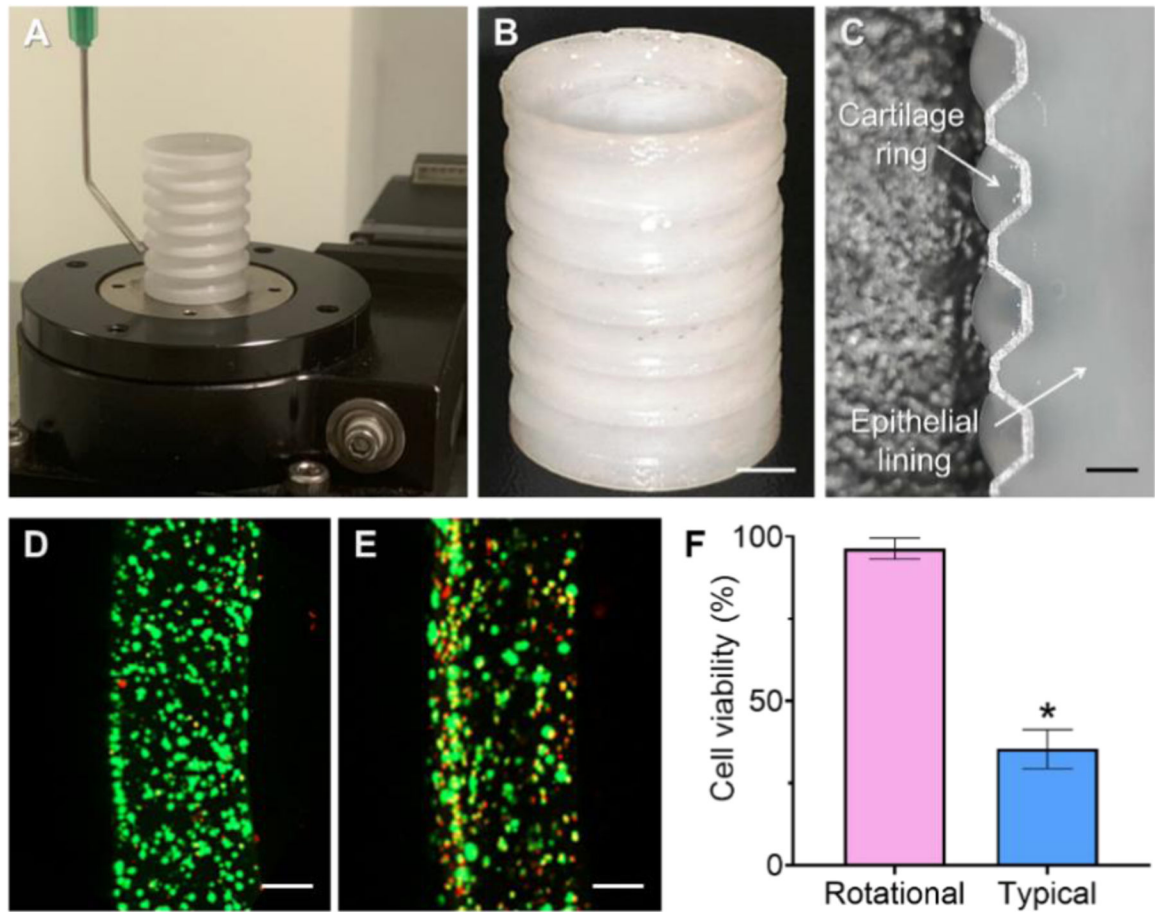
Fig. 3.
Rotational printing of separate cartilage rings and epithelial lining. (A) Photograph of rotational printing process. (B) Trachea-mimetic cellular construct after rotational printing. Scale bar, 5 mm. (C) Longitudinal cross-section of a trachea-mimetic cellular construct along with an interior surface. Scale bar, 1 mm. Radial cross-section of cartilage ring stained for live and dead cells from (D) rotational printing strategy and (E) typical printing strategy. Scale bars, 200 μm. (F) Cell viability according to different printing strategies. *p<0.01.
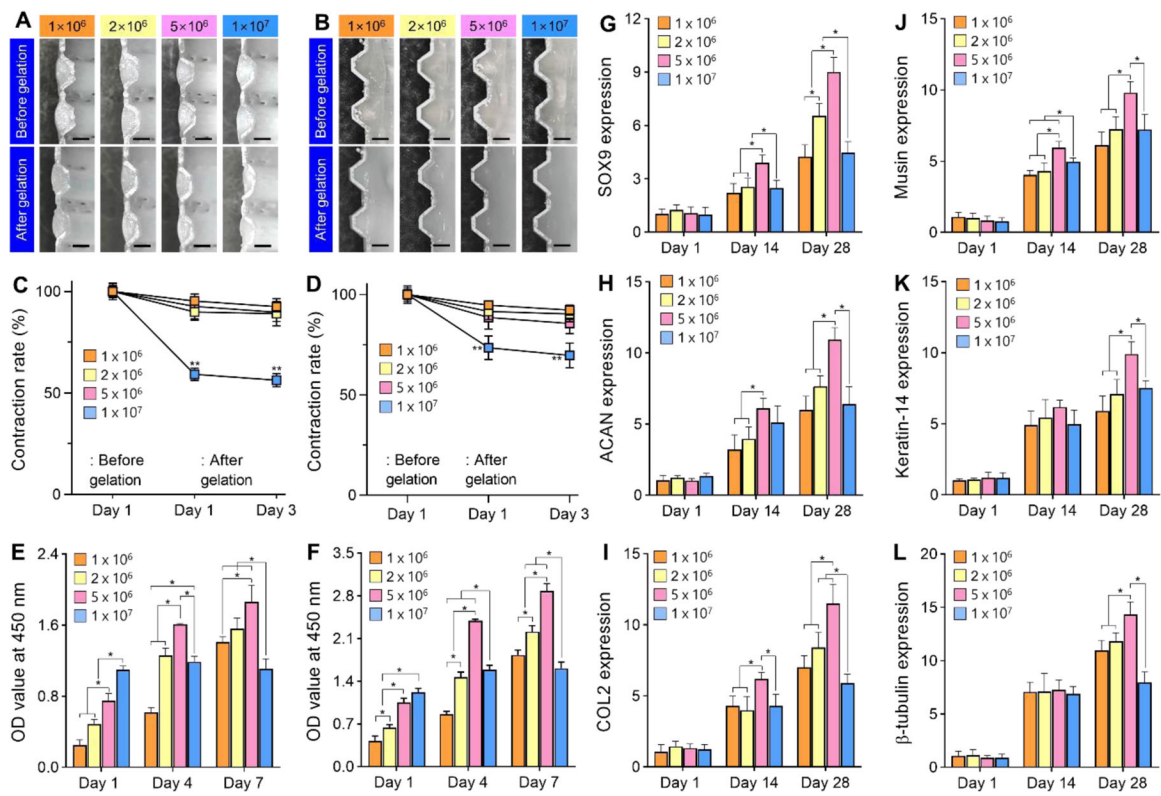
Fig. 4.

Cell density effect on the biological performance of cartilage rings and epithelial lining. Longitudinal cross-sections of (A) cartilage rings and (B) epithelial lining of tracheal construct with different cell densities before and after gelation. Scale bars, 10 mm. Volume contraction rate on (C) cartilage rings and (D) epithelial lining over time in culture for 3 days. Proliferation of (C) hNCs in cartilage rings and (F) hNTSCs in epithelial lining with different cell densities for 7 days of culture. Gene expression levels of cellular tracheal constructs with different cell densities for 28 days of culture using chondrogenic representative markers of (G) SOX9, (H) ACAN, and (I) COL2 and epithelial markers of (J) Musin, (K) Keratin-14, and (L) β-tubulin. *p<0.01. **p<0.01 when compared with the other groups.
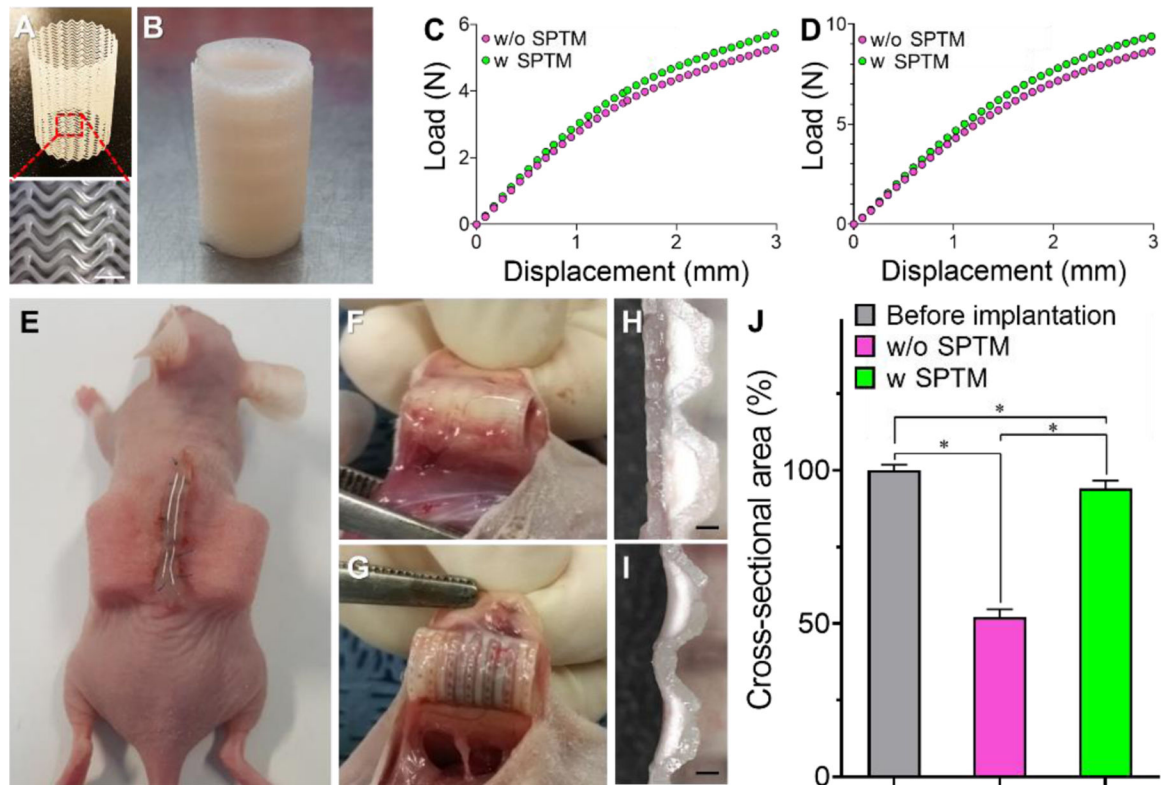
Fig. 5.
Prevention of cartilage rings resorption *in vivo*. (A) Photograph of SPTM. (B) Photograph of a trachea-mimetic cellular construct wrapping with SPTM. Scale bar, 1 mm. Load-displacement curves of trachea-mimetic constructs with or without SPTM under (C) three-point bending and (D) radial compression. (E) Subcutaneous implantation of trachea-mimetic constructs with or without SPTM wrapping. Retrieval of trachea-mimetic tracheal construct (F) with and (G) without SPTM wrapping after 8 weeks of implantation. Longitudinal cross-section of cartilage rings of retrieved trachea-mimetic construct (H) with and (I) without wrapping of SPTM at 8 weeks after implantation. Scale bars, 1 mm. (J) Cross-sectional area of cartilage rings from trachea-mimetic constructs before implantation and retrieved trachea-mimetic constructs after 8 weeks of implantation. *p<0.01.
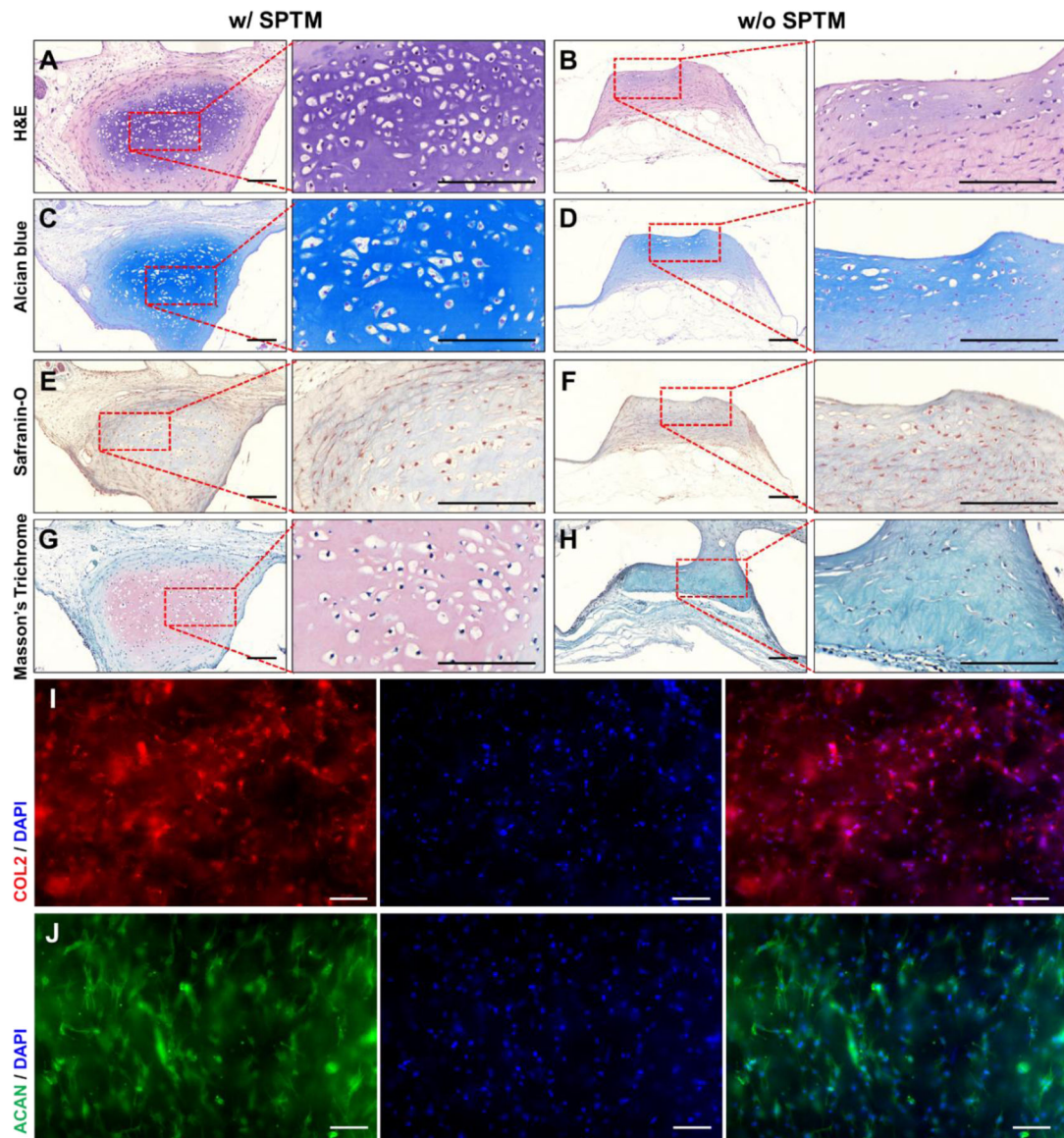
Fig. 6.
Evaluation of cartilage formation of trachea-mimetic cellular construct *in vivo*. (A, B) The H&E, (C, D) Alcian Blue, (E, F) Safranin-O, and (G, H) Masson's Trichrome staining result of longitudinal cross-section of cartilage rings from retrieved cellular constructs with (left) and without (right) wrapping of SPTM after 8 weeks of implantation. Scale bars, 500 μm. The immunofluorescence image of (I) COL2 and (J) ACAN in the retrieved trachea-mimetic cellular tracheal construct with wrapping of SPTM after 8 weeks of implantation. Scale bars, 200 μm.